

Harmonic microscopy of isotropic and anisotropic microstructure of the human cornea

Nicolas Olivier,¹ Florent Aptel,^{2,3} Karsten Plamann,²
Marie-Claire Schanne-Klein,¹ and Emmanuel Beaufreire^{1*}

¹Laboratory for optics and biosciences, Ecole Polytechnique ParisTech, CNRS,
and INSERM U696, 91128 Palaiseau, France,

²Laboratoire d'optique appliquée, ENSTA ParisTech, CNRS, 91761 Palaiseau, France,

³Lab. biotechnologie et oeil, Université Paris V, Hôpital Hôtel-Dieu, 75181 Paris, France

[*emmanuel.beaufreire@polytechnique.edu](mailto:emmanuel.beaufreire@polytechnique.edu)

Abstract: In this study we present combined third-harmonic generation (THG) and second-harmonic generation (SHG) microscopy images of intact human corneas, and we analyze experimentally and theoretically the origin of the THG signal. Multiharmonic microscopy provides detailed images of the cornea microstructure over its entire thickness. A component of the THG signal originates from cellular structures and another one originates from anisotropy changes between successive collagen lamellae in the stroma. This anisotropy-related signal can be specifically detected using circular incident polarization, and provide contrasted images of the stacking and tissue-scale heterogeneity of stromal lamellae. Forward-radiated THG and SHG signals are generally anticorrelated, indicating that maximum THG is obtained from lamellar interfaces whereas maximum SHG is obtained from within lamellae. Polarization-resolved THG imaging reflects the alternate anisotropy directions of the lamellae. We present a model for THG imaging of layered anisotropic samples and numerical calculations that account for our observations.

© 2010 Optical Society of America

OCIS codes: (180.4315) Nonlinear microscopy; (190.4160) Multiharmonic generation; (170.3880) Medical and biological imaging; (170.4470) Ophthalmology; (170.6935) Tissue characterization; (190.4710) Optical nonlinearities in organic materials.

References and links

1. W. Zipfel, R. Williams, and W. Webb, Nonlinear magic: multiphoton microscopy in the biosciences, *Nat. Biotechnol.* **21**(11), 1369–1377 (2003).
2. T. Nishida, Cornea, in *Cornea, 2nd edition*, E. H. J.H. Krachmer, M.J. Mannis, ed., pp. 3–26 (Elsevier Mosby, 2005).
3. W. Drexler and J. Fujimoto, State-of-the-art retinal optical coherence tomography, *Prog. Retin. Eye Res.* **27**(1), 45–88 (2008).
4. I. Jalbert, F. Stapleton, E. Papas, D. Sweeney, and M. Coroneo, In vivo confocal microscopy of the human cornea, *Br. J. Ophthalmol.* **87**, 225–36 (2003).
5. N. Morishige, A. Wahlert, M. Kenney, D. Brown, K. Kawamoto, T. Chikama, T. Nishida, and J. Jester, Second-harmonic imaging microscopy of normal human and keratoconus cornea, *Invest. Ophthalmol. Vis. Sci.* **48**(3), 1087–94 (2007).
6. F. Aptel, N. Olivier, A. Deniset-Besseau, J.-M. Legeais, K. Plamann, M.-C. Schanne-Klein, and E. Beaufreire, Multimodal nonlinear imaging of the human cornea, *Invest. Ophthalmol. Vis. Sci.* **51** (2010, in press).

7. D. W. Piston, B. R. Masters, and W. W. Webb, 3-Dimensionally Resolved Nad(P)H Cellular Metabolic Redox Imaging of the in-Situ Cornea with 2-Photon Excitation Laser-Scanning Microscopy, *J. Microsc.-Oxford* **178**, 20–27 (1995).
8. J. Lyubovitsky, J. Spencer, T. Krasieva, B. Andersen, and B. Tromberg, Imaging corneal pathology in a transgenic mouse model using nonlinear microscopy, *J. Biomed. Opt.* **11**(1), 014013 (2006).
9. S.-W. Teng, H.-Y. Tan, J.-L. Peng, H.-H. Lin, K. Kim, W. Lo, Y. Sun, W.-C. Lin, S.-J. Lin, S.-H. Jee, P. So, and C.-Y. Dong, Multiphoton autofluorescence and second-harmonic generation imaging of the ex vivo porcine eye, *Invest. Ophthalmol. Vis. Sci.* **47**(3), 5251–5259 (2006).
10. B.-G. Wang, K. Koenig, I. Riemann, R. Krieg, and K.-J. Halbhuber, Intraocular multiphoton microscopy with subcellular spatial resolution by infrared femtosecond lasers, *Histochem. Cell. Biol.* **126**(4), 507–515 (2006).
11. M. Han, G. Giese, and J. F. Bille, Second harmonic generation imaging of collagen fibrils in cornea and sclera, *Opt. Express* **13**(15), 5791–5797 (2005).
12. A. Yeh, N. Nassif, A. Zoumi, and B. Tromberg, Selective corneal imaging using combined second-harmonic generation and two-photon excited fluorescence, *Opt. Lett.* **27**(23), 2082–2084 (2002).
13. Q. F. Wu and A. T. Yeh, Rabbit cornea microstructure response to changes intraocular pressure visualized by using nonlinear optical microscopy, *Cornea* **27**(2), 202–208 (2008).
14. P. Matteini, F. Ratto, F. Rossi, R. Cicchi, C. Stringari, D. Kapsokalyvas, F. S. Pavone, and R. Pini, Photothermally-induced disordered patterns of corneal collagen revealed by SHG imaging, *Opt. Express* **17**(6), 4868–4878 (2009).
15. L. Jay, A. Brocas, K. Singh, J.-C. Kieffer, I. Brunette, and T. Ozaki, Determination of porcine corneal layers with high spatial resolution by simultaneous second and third harmonic generation microscopy, *Opt. Express* **16**(21), 16284–16293 (2008).
16. S. Y. Chen, H. C. Yu, I. J. Wang, and C. K. Sun, Infrared-based third and second harmonic generation imaging of cornea, *J. Biomed. Opt.* **14**(4), 044012 (2009).
17. R. Williams, W. Zipfel, and W. Webb, Interpreting second-harmonic images of collagen I fibrils, *Biophys. J.* **88**, 1377–1386 (2005).
18. M. Strupler, A.-M. Pena, M. Hernest, P.-L. Tharoux, J.-L. Martin, E. Beaurepaire, and M.-C. Schanne-Klein, Second harmonic imaging and scoring of collagen in fibrotic tissues, *Opt. Express* **15**(7), 4054–4065 (2007).
19. X. Han, R. M. Burke, M. L. Zettel, P. Tang, and E. B. Brown, Second harmonic properties of tumor collagen: determining the structural relationship between reactive stroma and healthy stroma, *Opt. Express* **16**(3), 1846–1859 (2008).
20. D. Débarre, W. Supatto, A.-M. Pena, A. Fabre, T. Tordjmann, L. Combettes, M.-C. Schanne-Klein, and E. Beaurepaire, Imaging lipid bodies in cells and tissues using third-harmonic generation microscopy, *Nat. Methods* **3**(1), 47–53 (2006).
21. R. Boyd, *Nonlinear optics, 3rd edition* (Academic Press, 2008).
22. Y. Barad, H. Eisenberg, M. Horowitz, and Y. Silberberg, Nonlinear scanning laser microscopy by third harmonic generation, *Appl. Phys. Lett.* **70**, 922–924 (1997).
23. M. Muller, J. Squier, K. R. Wilson, and G. Brakenhoff, 3D-microscopy of transparent objects using third-harmonic generation, *J. Microsc.* **191**, 266–274 (1998).
24. D. Débarre, W. Supatto, and E. Beaurepaire, Structure sensitivity in third-harmonic generation microscopy, *Opt. Lett.* **30**(16), 2134–2136 (2005).
25. D. Débarre and E. Beaurepaire, Quantitative characterization of biological liquids for third-harmonic generation microscopy, *Biophys. J.* **92**(2), 603–612 (2007).
26. D. Oron, D. Yelin, E. Tal, S. Raz, R. Fachima, and Y. Silberberg, Depth-resolved structural imaging by third-harmonic generation microscopy, *J. Struct. Biol.* **147**(1), 3–11 (2004).
27. W. Supatto, D. Débarre, B. Moulia, E. Brouzés, J.-L. Martin, E. Farge, and E. Beaurepaire, In vivo modulation of morphogenetic movements in *Drosophila* embryos with femtosecond laser pulses, *Proc. Nat. Acad. Sci. USA* **102**(4), 1047–1052 (2005).
28. S.-P. Tai, W.-J. Lee, D.-B. Shieh, P.-C. Wu, H.-Y. Huang, C.-H. Yu, and C.-K. Sun, In vivo optical biopsy of hamster oral cavity with epi-third-harmonic generation microscopy, *Opt. Express* **14**(13), 6178–6187 (2006).
29. D. Oron, E. Tal, and Y. Silberberg, Depth-resolved multiphoton polarization microscopy by third-harmonic generation, *Opt. Lett.* **28**(23), 2315 (2003).
30. R. W. Knighton, X. R. Huang, and L. A. Cavuoto, Corneal birefringence mapped by scanning laser polarimetry, *Opt. Express* **16**(18), 13,738–13,751 (2008).
31. J.-X. Cheng and X. Xie, Green's function formulation for third harmonic generation microscopy, *J. Opt. Soc. Am. B* **19**(7), 1604–1610 (2002).
32. N. Olivier and E. Beaurepaire, Third-harmonic generation microscopy with focus-engineered beams: a numerical study, *Opt. Express* **16**(19), 14,703–14,715 (2008).
33. A. Vogel, J. Noack, G. Huttman, and G. Paltauf, Mechanisms of femtosecond laser nanosurgery of cells and tissues, *Appl. Phys. B-Lasers O.* **81**(8), 1015–1047 (2005).
34. H. Soong and J. Malta, Femtosecond lasers in ophthalmology, *Am. J. Ophthalmol.* **147**(2), 189–197 (2009).

1. Introduction

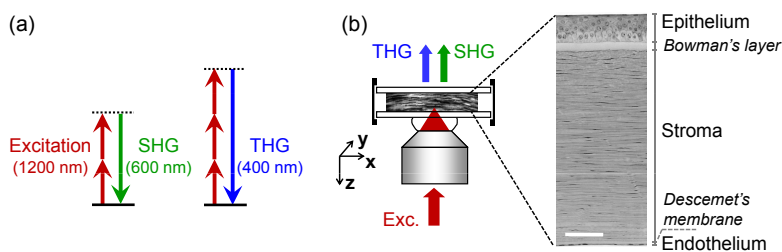


Fig. 1. Imaging method. (a) Principles of multiharmonic microscopy, and wavelengths involved. (b) Right: Experimental geometry. In this study, intact excised corneas were mounted between glass coverslips, illuminated from the endothelial side, and imaged in transmission. Left: histological image of a human cornea, shown for comparison with the THG-SHG images. Scale bar 100 μm .

Multiphoton (or nonlinear) microscopy (MPM) is an effective method for obtaining virtual biopsies from intact tissue [1]. One specific advantage of MPM is that several mechanisms such as fluorescence and harmonic generation can be combined to visualize different endogenous sources of contrast, providing structural and biochemical information on unstained samples not accessible to other noninvasive methods. This multimodal capability is particularly attractive for visualizing the microstructure of highly organized tissues such as the cornea: corneas consist of a stratified epithelium composed of 5-7 cell layers, a stroma composed of $\approx 2\mu\text{m}$ -thick collagen lamellae stacked in a plywood-like organization harboring sparsely distributed keratocytes, and an endothelium (see Fig. 1) [2]. Alternatively, linear optical imaging techniques such as optical coherence tomography (OCT) [3] and confocal reflectance microscopy [4] are often used for obtaining *in situ* ophthalmic images. However, as their contrast mechanism relies on spatial variations of refractive indices, linear techniques may sometimes offer limited contrast and specificity. This motivated a number of studies investigating the application of multiphoton microscopy to human [5, 6] and animal corneas (e.g. [7–16]). Two-photon-excited fluorescence (2PEF) imaging with 730-900 nm excitation reveals the distribution of endogenous chromophores [6–10], whereas second-harmonic generation (SHG), that is obtained from dense noncentrosymmetrical structures such as collagen fibrils [17–19], reveals collagen lamellae in the corneal stroma [5, 6, 9, 11–16]. Third-harmonic generation (THG) is easily combined with SHG and 2PEF [6, 20] and provides an additional contrast mechanism. Unlike SHG, THG does not require asymmetry and can be obtained from any medium. However no THG is observed from homogeneous normally dispersive media, as the Gouy axial phase shift of the excitation beam near focus results in destructive interference [21]. THG microscopy therefore detects optical inhomogeneities with size comparable to the beam focus [22–24]. At the interface between two media a and b , the detected intensity approximately scales as $(\alpha_a - \alpha_b)^2$ where $\alpha = \chi^{(3)}/n\Delta n$, $\chi^{(3)}$ is the third-order nonlinear susceptibility, n is the refractive index at the harmonic frequency and Δn is the dispersion [25]. This nonlinear mechanism produces contrasted images where heterogeneities emerge over a dark background. In particular, a strong signal is obtained at the interface between an aqueous medium and a lipidic, mineralized or absorbing organelle a few 100s of nm in size [20, 25] and THG imaging can be used to visualize the morphology of unstained tissues and embryos [26–28]. Besides this basic contrast mechanism, one often overlooked aspect of THG is that it can be used to probe microscopic anisotropy and birefringence using appropriate polarization of the excitation beam, as demonstrated in biogenic calcite crystals [29].

In the present study we expand on our previous investigation of THG-SHG-2PEF imaging of intact human corneas [6], by analyzing experimentally and theoretically the origin of the THG signal. We show that one component of the THG signal originates from cell structures and another one originates from anisotropy changes between successive collagen lamellae in the stroma. We show that this anisotropy-related signal can be specifically detected using circular incident polarization, and that polarization-resolved THG imaging reflects the alternate anisotropy directions of the lamellae. We find that forward-radiated THG and SHG signals are generally anticorrelated, suggesting that THG is obtained from lamellar interfaces whereas SHG is maximized inside lamellae. Finally, we derive a model for THG imaging of layered anisotropic samples and perform numerical calculations that account for our experimental observations.

2. THG/SHG imaging of entire human corneas

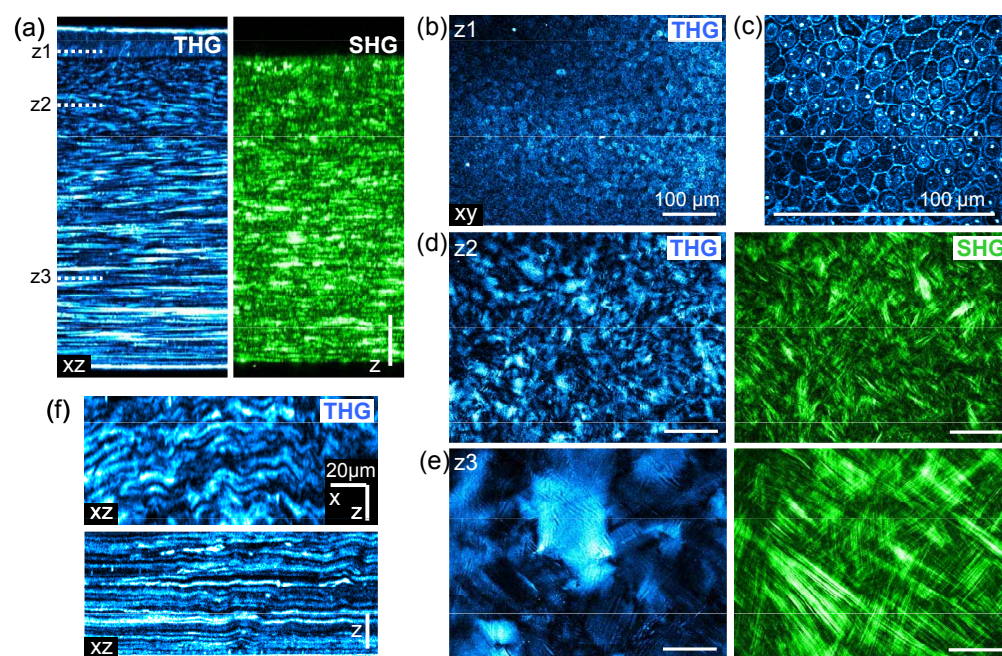


Fig. 2. THG/SHG imaging of human corneas showing organization at different depths. (a) and (Media 1) XZ reprojection of a series of THG-SHG images. $NA \approx 0.75$; Z-step size = $2 \mu m$; scale bars $20 \mu m(X) \times 100 \mu m(Z)$. (b) THG image of the epithelium recorded at the depth indicated in (a). Scale bar $100 \mu m$. (c) Higher resolution ($NA = 1.2$) THG image showing signals from nucleus-cytoplasm and cell-cell interfaces. Scale bar $100 \mu m$. (d, e) and (Media 2) THG-SHG images recorded at the depths indicated in (a) showing different stroma organizations. Scale bar $100 \mu m$. (f) and (Media 3) XZ reprojections of high resolution ($NA = 1.2$) THG stacks showing collagen lamellae organization in the anterior (top) and posterior (bottom) stroma. Z-step size = $0.5 \mu m$; scale bars $20 \mu m$.

Fresh intact corneas were mounted between two coverslips and THG-SHG imaging was performed in transmission with 1200 nm excitation, as shown in Fig. 1 and detailed in the Appendix at the end of the article. In non-edematous (transparent) corneas, THG-SHG images could be recorded over the entire corneal thickness with little loss in resolution (0.75 NA excitation). An example of integral imaging with linear incident polarization is shown in Fig. 2,

(Media 1) and (Media 2). In the following, we briefly describe the signals obtained from isotropic (cells) and anisotropic (stroma) structures using linear incident polarization, before discussing polarization sensitivity in the next section.

Representative THG images of the corneal epithelium are presented in Fig. 2(b), 2(c). High NA THG images provide a detailed view of the epithelium architecture, where cellular and nuclear interfaces are visible [Fig. 2(c)]. Since no THG signal can be obtained from a homogeneous isotropic medium with normal dispersion [22], these signals result from sub- μm bulk heterogeneity. Nuclear membrane visibility results from optical contrast between nuclei and cytoplasm, creating an interface between two bulk media. Cell-cell interface signals have a different nature and can only be explained by the presence of a sizable "slab" of intercellular medium, consistent with the structure of the corneal epithelium [2]. We note that such a signal may be modulated by applying an osmotic stress to the cornea causing tissue swelling around cells [6]. Similar structures are visible in the endothelium [6].

The corneal stroma is composed of stacked $\approx 2\text{-}\mu\text{m}$ -thick lamellae parallel to the surface of the cornea (xy orientation) harboring sparsely distributed keratocytes [2]. The lamellae are composed of thin collagen fibrils incorporated in a ground substance, that are aligned along a quasi-hexagonal lattice. Adjacent lamellae exhibit perpendicular fibril orientation. As discussed in several studies, SHG signals originating from the fibrillar collagen are observed in the stroma. Forward-detected SHG images exhibit striated features that likely reflect the orientation and distribution of the fibrils [see Fig. 2(d), 2(e) and Fig. 3]. However, since individual fibrils are not resolved because of their small diameter (35 nm) and dense packing, second-harmonic radiation results from complex interference processes.

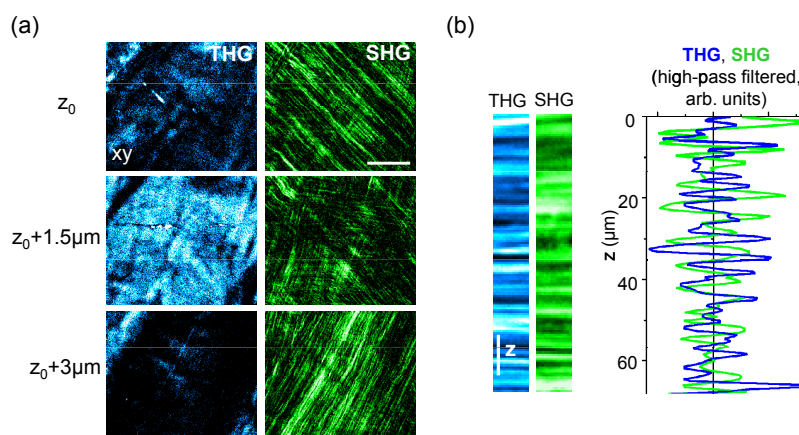


Fig. 3. Anticorrelation of THG and SHG maxima in the stroma. (a) High-resolution (1.2 NA excitation) THG/SHG images recorded at successive depths in the stroma illustrating the difference between the two signals (see text). Scale bar $20\ \mu\text{m}$. (b) Reprojection and profile along the optical axis of a stack recorded with $0.5\ \mu\text{m}$ axial increment. Scale bar $10\ \mu\text{m}$.

Interestingly, the THG signal provides complementary information. In particular, the stacked organization of the lamellae is uniquely revealed in xz -projected THG images, as illustrated in Fig. 2(f). Combined THG-SHG imaging therefore provides a multiscale description of the stromal organization, and reveals variations of the large-scale organization of the collagen lamellae at successive depths [see Fig. 2(d), 2(e). The posterior region of the stroma typically exhibits a regular, long-range stacked organization differing from the anterior region [Fig. 2(f) and (Media 3)]. Additionally, we observed in high resolution (1.2 NA) images that THG and SHG signal maxima were generally anticorrelated and that THG signal maxima often correspond to

a change of orientation of the SHG image pattern (Fig. 3). These observations suggest that THG signals are obtained at the interfaces between lamellae, whereas strongest SHG is obtained inside lamellae.

3. Polarization-sensitive THG imaging of the stroma

The imaging experiments described above were performed with linearly polarized laser light. Indeed, the induced third-harmonic polarization vanishes in the case of isotropic media illuminated with circularly polarized light, even in the presence of heterogeneity [29]. This stems from the fact that the $\chi^{(3)}$ tensor responsible for the THG response of a homogeneous isotropic medium reduces to: [21]

$$\chi_{ijkl}^{(3)} = \chi_0(\delta_{ij}\delta_{kl} + \delta_{ik}\delta_{jl} + \delta_{il}\delta_{jk}) \quad (1)$$

where χ_0 is constant and δ is the Kronecker delta. The third-harmonic nonlinear polarization generated by a field $\mathbf{E} = (E_x, E_y, E_z)$ in an isotropic media can then be expressed as :

$$\mathbf{P}^{(3\omega)} = \chi_0 \begin{bmatrix} E_x(E_x^2 + E_y^2 + E_z^2) \\ E_y(E_x^2 + E_y^2 + E_z^2) \\ E_z(E_x^2 + E_y^2 + E_z^2) \end{bmatrix} \quad (2)$$

In the case of circular incident polarization (*i.e.* $E_y = iE_x$), the nonlinear polarization $\mathbf{P}^{(3\omega)}$ is null and no THG is observed.

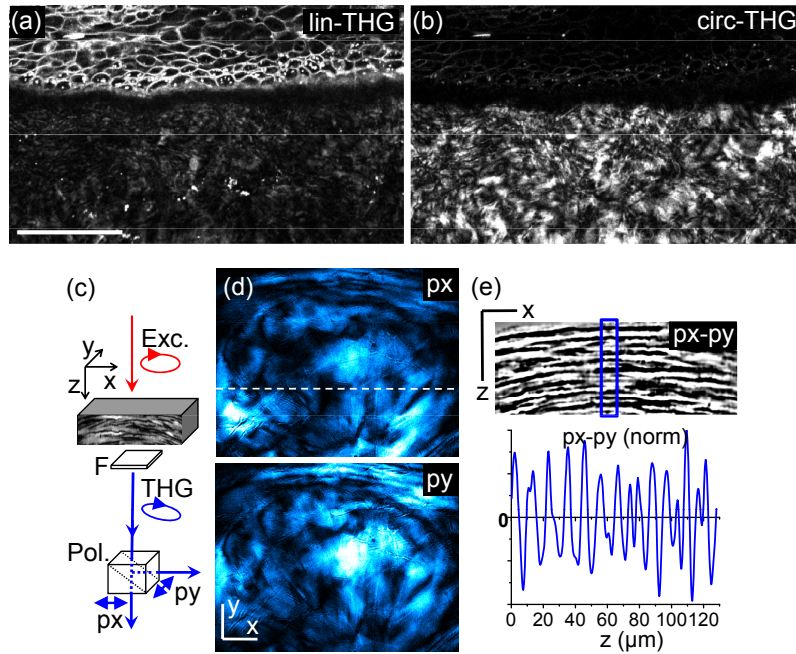


Fig. 4. Polarization-sensitive THG imaging. (a-b) THG imaging of a cornea with (a) linear and (b) circular incident polarization reveals different structures because circ-THG specifically detects anisotropy. Scale bar $100 \mu\text{m}$. (c) Principle of the experiment with polarization-resolved detection. (d,e) THG imaging of the stroma with circular incident polarization and polarization-resolved detection. Scale bars $100 \mu\text{m}$.

Conversely, it has been shown that strongly birefringent media such as calcite can efficiently produce THG with both linearly and circularly polarized excitation [29]. The case of the lay-

ered corneal stroma is slightly more complex: lamellae may be viewed as stacked slabs with alternate anisotropy directions (noted x and y). When the excitation beam (propagating along direction z) is focused near the interface between two xy lamellae, harmonic light from the first lamella emerges with a polarization state different from the one from the second lamella. As a consequence, Gouy-shift-induced destructive interference is not complete even if birefringence is weak, as detailed in section 4. Excitation with circular polarization is therefore a means to specifically detect anisotropy variations.

In Fig. 4(a), 4(b), a section of the anterior stroma was imaged using THG with linear incident polarization (lin-THG) and THG with circular incident polarization (circ-THG). The two images are obviously different. Lin-THG reveals cellular structures (epithelial cells and stromal keratocytes) and a weaker component from the stromal lamellae. Circ-THG is obtained specifically from the lamellae. When going from linear to circular excitation, cell signals are decreased by a factor ≈ 20 while lamellae signals are increased 2-3 times, providing a convenient means to distinguish the two contributions.

More information can be obtained by recording polarization-resolved THG images. We used circular incident polarization and recorded two orthogonally-polarized images p_x and p_y [Fig. 4(c), 4(d)]. Figure 4(e) shows that the difference between these polarization-resolved images exhibit sign changes as a function of z . This measurement reflects the alternate directions of the anisotropy axes, as discussed in the next section.

4. Model of THG from a layered anisotropic sample

In this section we derive a simple model for THG imaging of the corneal stroma that accounts for the previous observations.

One first observation is that the microscopic anisotropy of the stroma is strong enough to be detected in THG images recorded with circular incident polarization [Fig. 4(b)], despite the fact that linear birefringence is weak [30]. The second observation is that the polarization of the radiated THG exhibits alternate ellipticity directions as the incident beam is focused in successive lamellae [Fig. 4(e)]. In the following, we consider THG from a layered sample consisting of anisotropic layers perpendicular to the optical axis of the microscope, excited by a focused Gaussian beam with linear or circular polarization. This is consistent with electron micrographs of corneal stroma which reveal a stacking of lamellae consisting of aligned collagen fibrils [2] along a quasi-hexagonal lattice: as a first approximation, each lamella may be viewed as an uniaxial crystal, with successive lamellae oriented along orthogonal directions. We first consider the case of a perfectly organized stroma consisting of lamellae of equal thickness and show that THG is observed principally at the interface between lamellae. We then consider the possibility of intra-lamellar organization heterogeneity along the z axis to account for polarization changes in the THG signal. Two aspects must be taken into account: tensor symmetries within xy layers, and phase matching along the z axis.

We make the following hypotheses and approximations (see Fig. 5 for geometry):

- Individual stromal lamellae exhibit hexagonal $6mm$ symmetry alternatively along x and y axis (*i.e.* orthogonal to the direction of propagation);
- We neglect refractive index dispersion and linear birefringence (*i.e.* $n_\omega = n_{3\omega}$ everywhere).

Our strategy is then to consider the x and y component of the nonlinear polarization independently, and to sum their contributions.

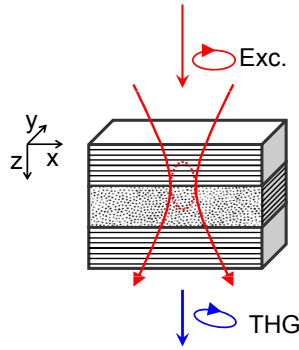


Fig. 5. Representation of our model stroma and imaging geometry.

4.1. THG from an anisotropic sample

The third-harmonic nonlinear polarization generated by a field $\mathbf{E} = (E_x, E_y, E_z)$ in a corneal lamella can be approximated as the polarization in a crystal with hexagonal $6mm$ symmetry around the x axis, and can be expressed as follows [21]:

$$\mathbf{P}^{(3\omega)} = \begin{bmatrix} E_x(\chi_{\parallel} E_x^2 + \chi_{cr} E_y^2 + \chi_{cr} E_z^2) \\ E_y(\chi_{cr} E_x^2 + \chi_{\perp} E_y^2 + \chi_{\perp} E_z^2) \\ E_z(\chi_{cr} E_x^2 + \chi_{\perp} E_y^2 + \chi_{\perp} E_z^2) \end{bmatrix} \quad (3)$$

where $\chi_{\parallel} = \chi_{xxxx}^{(3)}$, $\chi_{cr} = 3\chi_{xyyy}^{(3)}$, $\chi_{\perp} = \chi_{yyyy}^{(3)} = 3\chi_{yyzz}^{(3)}$ are the three independent tensorial components of the third-order susceptibility. In practical situations, we can generally neglect the z component of the excitation field [31, 32] and write:

$$\mathbf{P}^{(3\omega)} = \begin{bmatrix} E_x(\chi_{\parallel} E_x^2 + \chi_{cr} E_y^2) \\ E_y(\chi_{cr} E_x^2 + \chi_{\perp} E_y^2) \\ 0 \end{bmatrix} \quad (4)$$

One well studied case is when $\chi_{cr} = \chi_{\parallel} = \chi_{\perp} = \chi_0$, corresponding to isotropic media. If the sample is homogeneous, no far-field THG signal is obtained because the Gouy phase shift experienced by the focused excitation beam produces destructive interference along the z axis. If the sample is heterogeneous (interface or inclusion near focus) and the incident polarization is linear, destructive interference is not complete and a THG signal is observed (see below). Conversely as mentioned in section 2.3, circular incident polarization ($E_y = iE_x$) yields null nonlinear polarization $\mathbf{P}^{(3\omega)}$ and no THG even from interfaces between two isotropic media.

4.2. Interface between an isotropic medium and air

We denote $G_0(\mathbf{r})$ the field distribution of a linearly x -polarized focused Gaussian beam, where \mathbf{r} is a point near focus. The nonlinear polarization created by this distribution in an isotropic medium can be expressed as:

$$\mathbf{P}^{(3\omega)}(\mathbf{r}) = G_0(\mathbf{r})^3 \begin{bmatrix} \chi_0 \\ 0 \\ 0 \end{bmatrix} \quad (5)$$

We denote $C_0(z)$ the THG signal obtained when the focus is z -scanned across the interface between an isotropic medium ($\chi^{(3)} = \chi_0$) and air ($\chi^{(3)} = 0$), where z is the distance between

the interface and the focal plane. This case has been investigated previously [31, 32] and is illustrated in Fig. 6(a).

4.3. Interface between an anisotropic medium and air

We now consider the case of an interface between air and the stroma [Fig. 6(b)], in the case of a Gaussian excitation with linear polarization making an angle θ with the main axis of the crystal. The nonlinear polarization in the anisotropic medium reads:

$$\mathbf{P}^{(3\omega)} = G_0^3 \begin{bmatrix} \cos\theta(\chi_{\parallel}\cos^2\theta + \chi_{cr}\sin^2\theta) \\ \sin\theta(\chi_{cr}\cos^2\theta + \chi_{\perp}\sin^2\theta) \\ 0 \end{bmatrix} \quad (6)$$

and the THG signal scales as:

$$I_{THG} \propto C_0(z) \left[\cos^2\theta |\chi_{\parallel}\cos^2\theta + \chi_{cr}\sin^2\theta|^2 + \sin^2\theta |\chi_{cr}\cos^2\theta + \chi_{\perp}\sin^2\theta|^2 \right] \quad (7)$$

In the case of a circularly polarized excitation, the nonlinear polarization in the anisotropic medium reads:

$$\mathbf{P}^{(3\omega)} = \frac{1}{2\sqrt{2}} G_0^3 \begin{bmatrix} (\chi_{\parallel} - \chi_{cr}) \\ i(\chi_{cr} - \chi_{\perp}) \\ 0 \end{bmatrix} \quad (8)$$

and the THG signal scales as $C_0(z)[|\chi_{\parallel} - \chi_{cr}|^2 + |\chi_{cr} - \chi_{\perp}|^2]$ [see Fig. 6(b)]. THG is circularly polarized if $\chi_{\parallel} = \chi_{\perp}$.

4.4. Interface between two semi-infinite layers with different orientations

We now consider the case of circularly polarized excitation only. We assume that the first layer is oriented along the x axis and the second one along the y axis, so the nonlinear polarization $\mathbf{P}_+^{(3\omega)}$ and $\mathbf{P}_-^{(3\omega)}$ created in the successive media can be expressed as:

$$\mathbf{P}_+^{(3\omega)} = \frac{G_0^3}{2\sqrt{2}} \begin{bmatrix} (\chi_{\parallel} - \chi_{cr}) \\ i(\chi_{cr} - \chi_{\perp}) \\ 0 \end{bmatrix} \quad (9)$$

$$\mathbf{P}_-^{(3\omega)} = \frac{G_0^3}{2\sqrt{2}} \begin{bmatrix} (\chi_{\perp} - \chi_{cr}) \\ i(\chi_{cr} - \chi_{\parallel}) \\ 0 \end{bmatrix} \quad (10)$$

Since no THG is obtained from a homogeneous medium, we obtain an equivalent system by adding $(\chi_{cr} - \chi_{\perp})G_0^3/2\sqrt{2}$ (resp. $i(\chi_{\perp} - \chi_{cr})G_0^3/2\sqrt{2}$) to the x (resp. y) polarization terms in both layers. We obtain:

$$\mathbf{P}_+^{(3\omega)} = \frac{G_0^3}{2\sqrt{2}} \begin{bmatrix} (\chi_{\parallel} - \chi_{\perp}) \\ 0 \\ 0 \end{bmatrix} \quad (11)$$

$$\mathbf{P}_-^{(3\omega)} = \frac{G_0^3}{2\sqrt{2}} \begin{bmatrix} 0 \\ i(\chi_{\perp} - \chi_{\parallel}) \\ 0 \end{bmatrix} \quad (12)$$

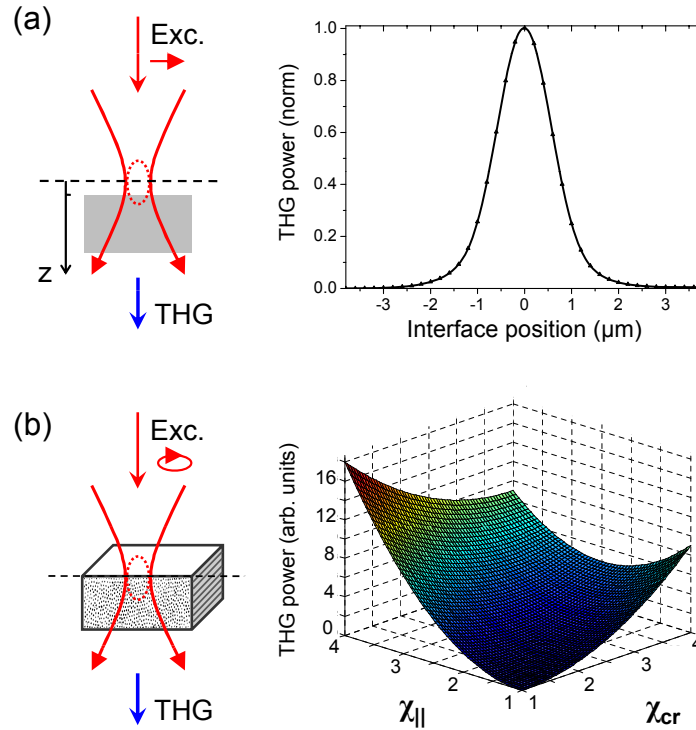


Fig. 6. Numerical calculations of THG at the interface between air and an isotropic or anisotropic medium. (a) THG power $C_0(z)$ obtained when the excitation beam is z -scanned across a xy interface between an isotropic medium and air. (b) THG power obtained with circular incident polarization at the interface between an anisotropic medium and air, as a function of the parameters χ_{\parallel} and χ_{cr} with $\chi_{\perp} = 1$ (see text). Notice that no signal is obtained in the case of an isotropic medium ($\chi_{\parallel} = \chi_{cr} = \chi_{\perp} = 1$). $NA=1.2$, $\lambda=1.2 \mu m$.

These expressions show that an interface between orthogonal lamellae behaves similarly to an interface between air and an anisotropic medium, yielding a signal proportional to $C_0(z) \cdot |\chi_{\parallel} - \chi_{\perp}|^2$ with circular polarization. The absence of χ_{cr} in this expression is not surprising, as this term couples the x and y polarization components and has a similar influence on both axes.

4.5. Polarization of the THG

In the sample geometry considered so far, a circularly polarized excitation beam always produces circularly polarized third-harmonic radiation, independently of the z -position of the interface. This does not reflect the alternate THG polarization directions observed experimentally [Fig. 7(a)]. The previous simple model is useful for understanding the interface nature of the observed THG radiation, but it does not account for the complexity of the stromal structure. For example electron micrographs [2] indicate that lamellae thickness is not constant, and that fibril stacking may present some disorder near interfaces. Therefore the third-order susceptibility tensor may not be constant within a lamella, and in some cases the excitation volume may encompass more than two lamellae. It would be a formidable task to analyze all the possible tensor geometries. However we can make the simple and realistic assumption that stromal lamellae are more organized in their center than near their interfaces so that χ_{\parallel} depends on the

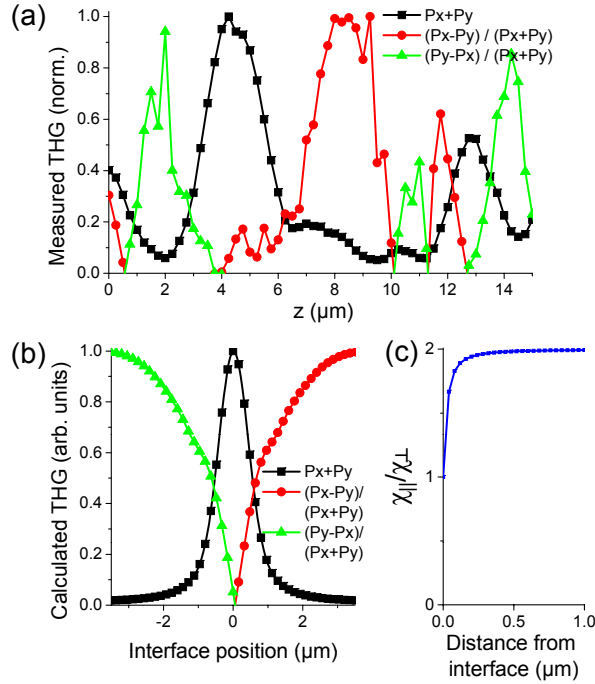


Fig. 7. Polarization-resolved THG: experiment and simulation. (a) z -profile of the total and polarization-resolved THG signal across a few stromal lamellae. Black squares represent the total THG signal. Red circles and green triangles correspond to regions where THG emission is elliptical. The total signal maxima ($z = 4$ and 13) and the ellipticity maxima are generally anticorrelated, even though the contrast is less clear when the lamellae are smaller than the axial resolution of the microscope (*e.g.* $z = 11$). (b) Numerical simulation for the case of an interface between two semi-infinite layers with different orientation, assuming that the interface is less structured than the interior of the layers (see text). (c) Distribution of $\chi_{\parallel} / \chi_{\perp}$ within a layer used for the simulation shown in (b) ($NA=1.2$, $\lambda=1.2 \mu\text{m}$).

axial (z) position within the lamella. The nonlinear polarization then reads:

$$\begin{aligned}
 \mathbf{P}_+^{(3\omega)} &= \begin{bmatrix} Ex(\chi_{\parallel}(z) \cdot Ex^2 + \chi_{cr} \cdot Ey^2 + \chi_{cr} \cdot Ez^2) \\ Ey(\chi_{cr} \cdot Ex^2 + \chi_{\perp} \cdot Ey^2 + \chi_{\perp} \cdot Ez^2) \\ Ez(\chi_{cr} \cdot Ex^2 + \chi_{\perp} \cdot Ey^2 + \chi_{\perp} \cdot Ez^2) \end{bmatrix} \\
 \mathbf{P}_-^{(3\omega)} &= \begin{bmatrix} Ex(\chi_{\perp} \cdot Ex^2 + \chi_{cr} \cdot Ey^2 + \chi_{\perp} \cdot Ez^2) \\ Ey(\chi_{cr} \cdot Ex^2 + \chi_{\parallel}(z) \cdot Ey^2 + \chi_{cr} \cdot Ez^2) \\ Ez(\chi_{\perp} \cdot Ex^2 + \chi_{cr} \cdot Ey^2 + \chi_{\perp} \cdot Ez^2) \end{bmatrix}
 \end{aligned} \quad (13)$$

where the z -component of the excitation field is no longer neglected.

Numerical simulations were performed using the approach described in [32]. If we assume that $\chi_{\perp} = \chi_{cr}$ and we consider a simple modulation where χ_{\parallel} is equal to $2\chi_{\perp}$ at the center of a lamella and to χ_{\perp} (*i.e.* isotropic case) at the interface [Fig. 7(c)], we find that the polarization of the THG radiation is also a function of z [Fig. 7(b)]. The THG signal is circularly polarized at the interface, and it is elliptically polarized within the lamellae with the main polarization component oscillating from one direction to the perpendicular one, in agreement with our polarization-resolved experiments. This confirms that a simple model of the stroma nonlinear

response accounts well for our experimental observations.

5. Conclusion

We have shown that multiharmonic microscopy provides detailed structural images of the human cornea. THG with linear and circular incident polarization produce fundamentally different images and can be used to separate contributions from isotropic and anisotropic microstructures. The isotropic component can be used to image cellular and anchoring structures, whereas the anisotropy-related THG signal reveals the stacking and tissue-scale heterogeneity of stromal lamellae with micrometer 3D resolution *i.e.* at the scale of individual lamellae. These nonlinear mechanisms produce remarkably contrasted images. We derived a model describing THG by a layered anisotropic medium, that properly accounts for our experimental observations. This analysis provides a framework for interpreting THG images of the stroma and for future studies. Indeed, Fig. 2 and Fig. 5 show that THG/SHG imaging gives access to multiscale information on the organization of the intact stroma not accessible to linear techniques. Additional work will be needed to fully understand the SHG corneal images and also relate them to structural parameters, based on the findings presented here. One perspective will be to relate such multimodal images to multiscale (dis)organization parameters in the context of corneal dystrophy. Another perspective will be to apply this methodology for imaging the intact eye based on intra-ocular backscattering of the forward-radiated signals, as shown in fixed mouse corneal tissue. [16] Finally, we recall that harmonic microscopy is compatible with other femtosecond laser-based techniques already being applied to the cornea, such as 2PEF imaging [5–8] and femtosecond pulse-induced ablation [27, 33, 34], so that multimodal imaging may be used to visualize the cornea microstructure after laser surgery.

Appendix: materials and methods

Microscopy. Imaging was performed on a custom-built laser scanning multiphoton microscope equipped with detection channels in the backward (epi) and forward (trans) directions. Excitation was performed using an optical parametric oscillator (OPO) (APE, Germany) synchronously pumped by an automated titanium:sapphire oscillator (Coherent, USA), and delivering a 80 MHz train of 100-150 fs pulses at the focus of the objective. The microscope incorporated galvanometer mirrors (GSI Lumonics), motorized water-immersion objectives (20× 0.95 numerical aperture (NA) and 60× 1.2 NA, Olympus, Japan), photon-counting photomultiplier modules (ET Enterprises Ltd., UK), lab-designed counting electronics, dichroic mirrors and spectral filters (Chroma Technology Corp, USA, and Semrock, USA). Scanning and signal acquisition were synchronized using LabView software and a multichannel I/O board (National Instruments, USA). As red-shifted excitation wavelengths were used for THG-SHG imaging (typ. 1200 nm), two-photon absorption by endogenous absorbers was minimized and higher pulse energies could be used while preserving cell and tissue integrity. Simultaneous THG/SHG imaging was performed with trans-detection of both signals. The incident polarization was controlled by inserting a polarizer and a quarter wave plate before the scanners. High-resolution images were recorded using a 1.2 NA 60× (water immersion) objective resulting in 1.2 μm axial resolution in THG images at the tissue surface (measured from a glass-water interface). Unless otherwise specified, larger-scale images were recorded using the 20× objective with its pupil underfilled (resulting in 0.75 effective NA) providing 3.5 μm axial (and sub- μm lateral) resolution in THG images. Power after the objective was typically 100 mW, and was adjusted with imaging depth to compensate for scattering-induced signal attenuation. Acquisition time was 3-20 $\mu\text{s}/\text{pixel}$.

Human corneas. The study was conducted according to the tenets of the Declaration of Helsinki and the French legislation for scientific use of human corneas. We analyzed fresh

human corneal buttons obtained from patients that underwent penetrating keratoplasty. Immediately after their removal, the whole trephined corneal buttons were placed in Hanks medium (Sigma-Aldrich, St. Louis, MO) supplemented with 5% Dextran T500 (Sigma-Aldrich) to avoid edema. Corneal buttons were maintained between two 150 μ m-thick glass coverslips to flatten the corneal surface and imaged from the endothelium side.

Acknowledgements

We gratefully acknowledge the Banque Francaise des Yeux (French Eye Bank) directed by P. Sabatier and the ophthalmology department at Hôtel-Dieu Hospital headed by G. Renard for the supply of human corneas. We thank M. Savoldelli for the histology, M. Strupler, G. Latour, D. Débarre, A. Deniset-Besseau, J.-M. Legeais, D. Peyrot, F. Deloison and J.-L. Martin for scientific discussions. This work was partly supported by Direction Générale de l'Armement (DGA).